Electronic Supplementary Information for

# Lateral and cross-lateral focusing of spherical particles in a square microchannel

by Yong-Seok Choi, Kyung-Won Seo and Sang-Joon Lee

## SI Figures

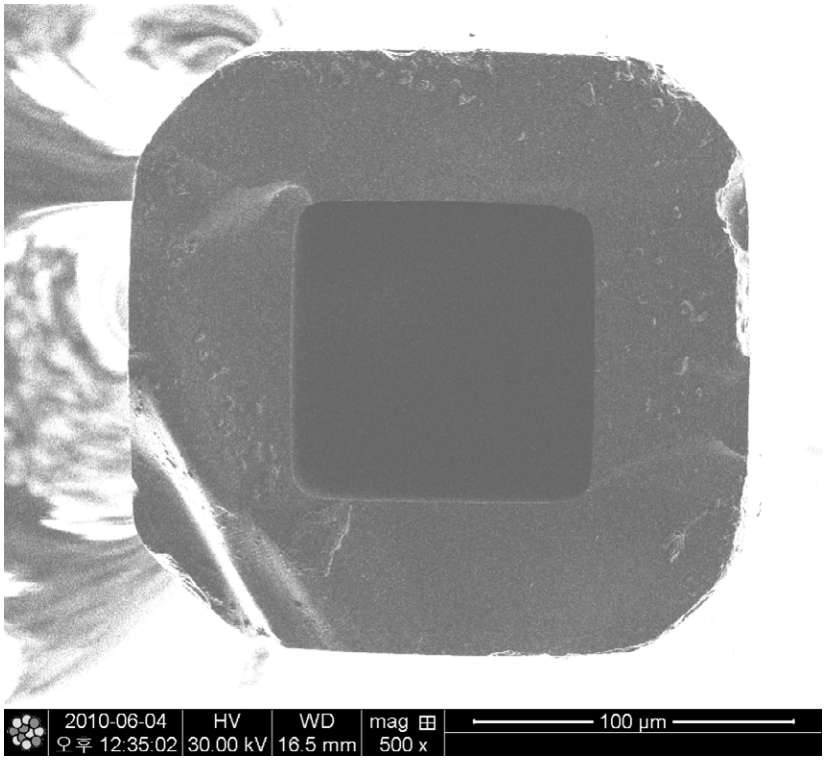


**Figure S1.** Cross-sectional view of the microchannel having hydraulic diameter of $H$ = 94.3 μm. The width and height of the channel are 94.8 and 93.7 μm, respectively. Although the four corners are slightly rounded, the cross-section was assumed as a regular square.

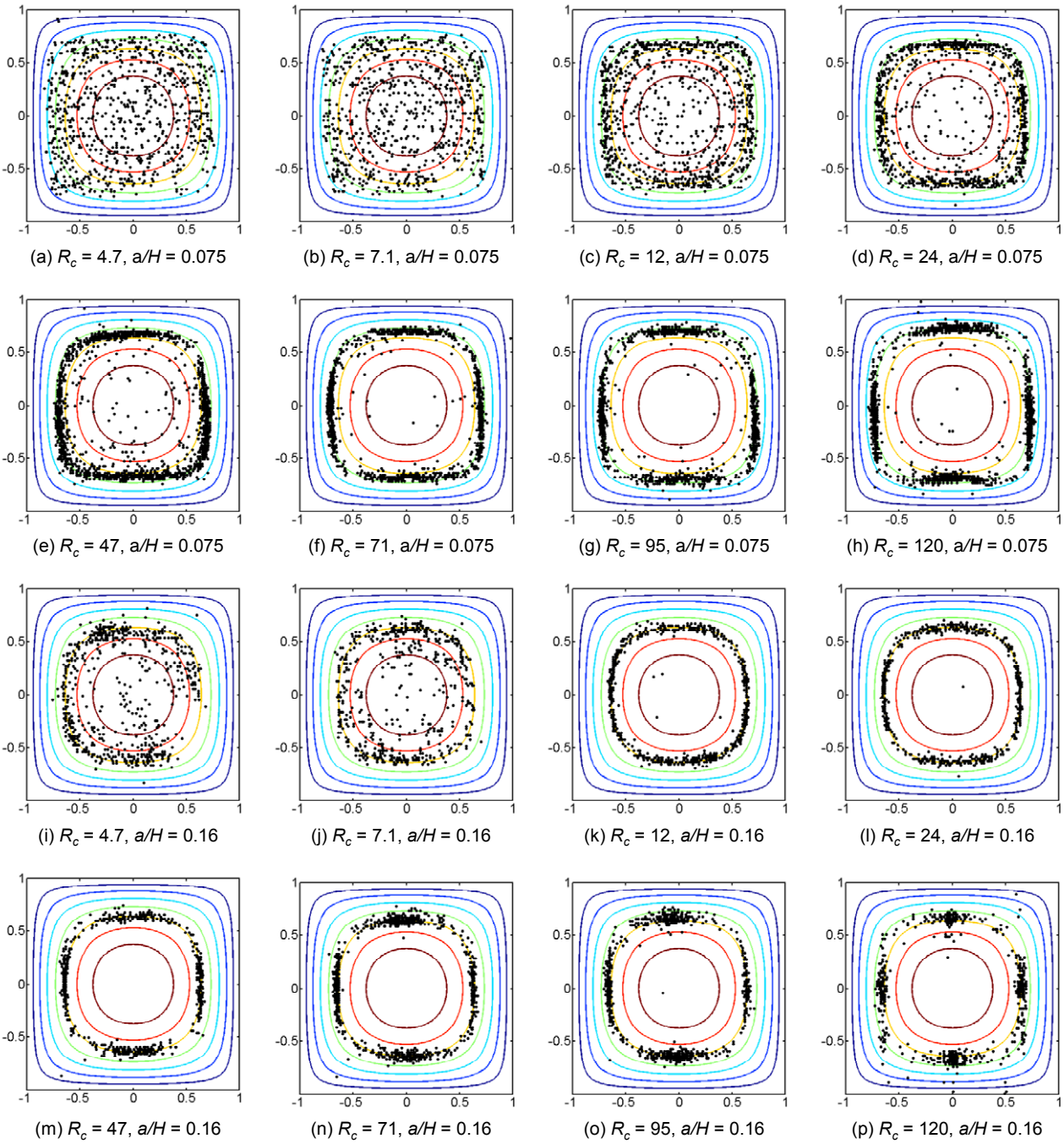


**Figure S2.** Cross-sectional distributions of the extracted particles. The width and height of the channel are normalized by the hydraulic radius $h$. As $R_C$ increases, the particles are focused in a certain radial position at first and then further focused into four equilibrium positions near the center of each channel face.

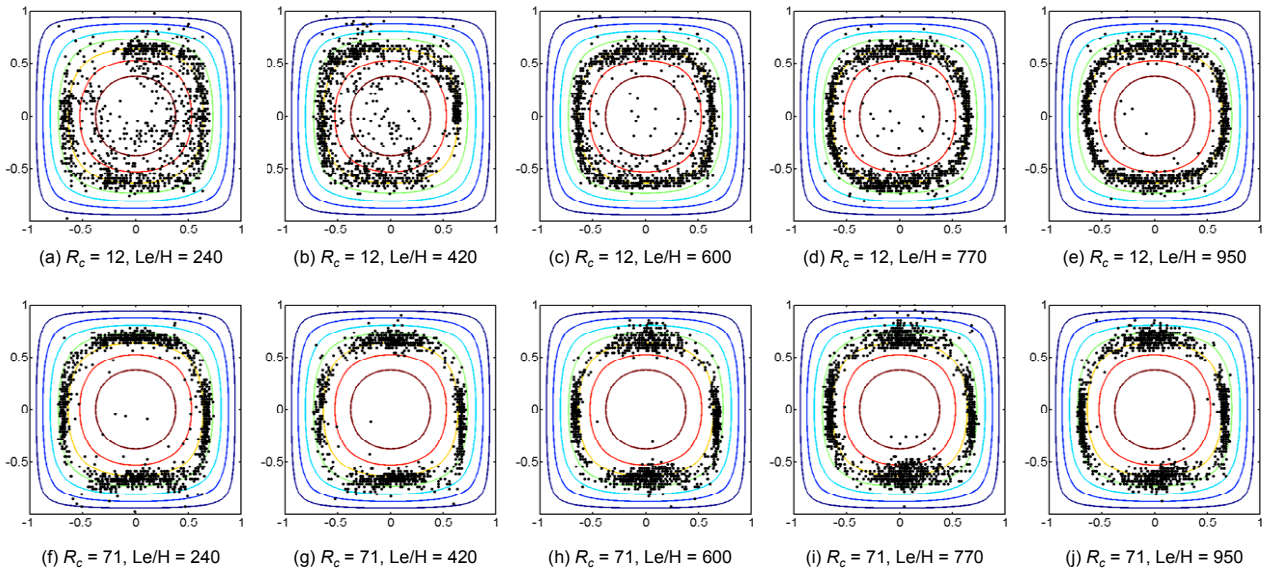


**Figure S3.** Cross-sectional distributions of the extracted particles for $a/H$ = 0.12. The width and height of the channel are normalized by the hydraulic radius $h$. As $L_E/H$ increases, the particles are focused at a certain equilibrium position.

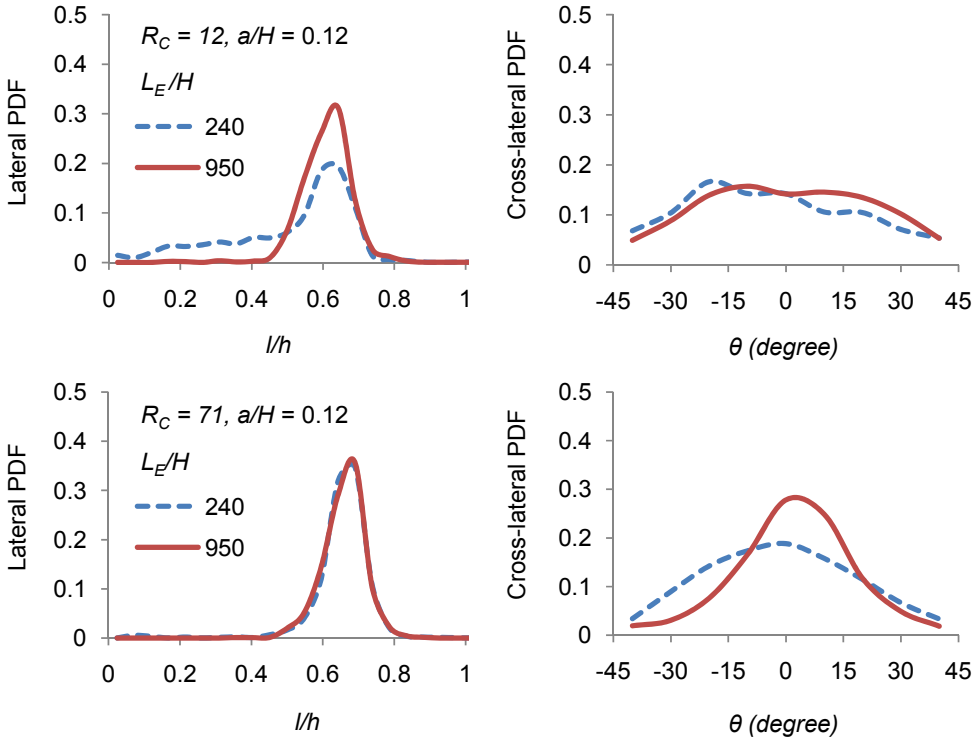


**Figure S4.** Lateral and cross-lateral probability density functions (PDFs) of the particles shown in Fig. S3 for $L_E/H$ = 240 and 950. For the case of $R_C$ = 12, a particle peak develops in the lateral PDF as $L_E/H$ increases. At higher value of $R_C$ = 71, a peak is also observed in the cross-lateral PDF around $\theta$ = 0 as $L_E/H$ increases. This cross-lateral focusing occurs when particles are fully focused at a certain lateral peak position.

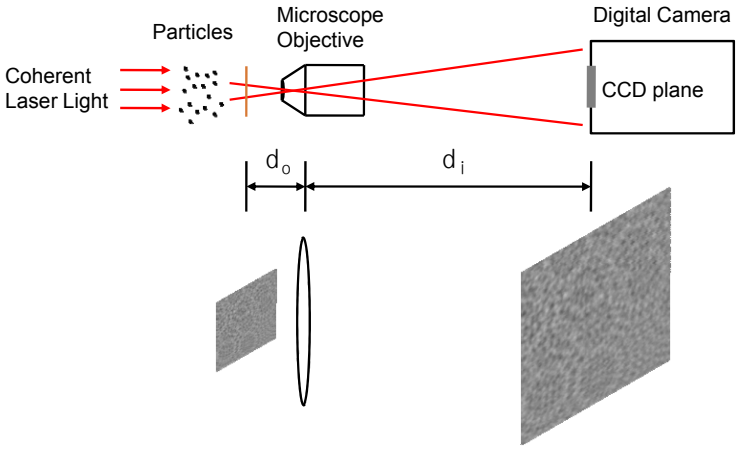


**Figure S5.** Optical setup for digital holographic microscopy and digital hologram acquisition

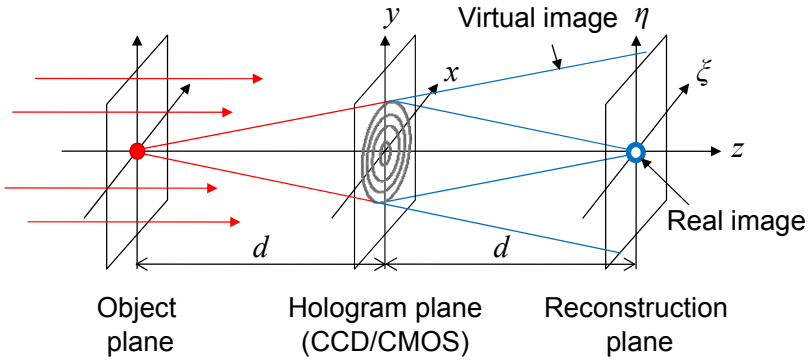


**Figure S6.** Coordinate systems for the numerical reconstruction procedure

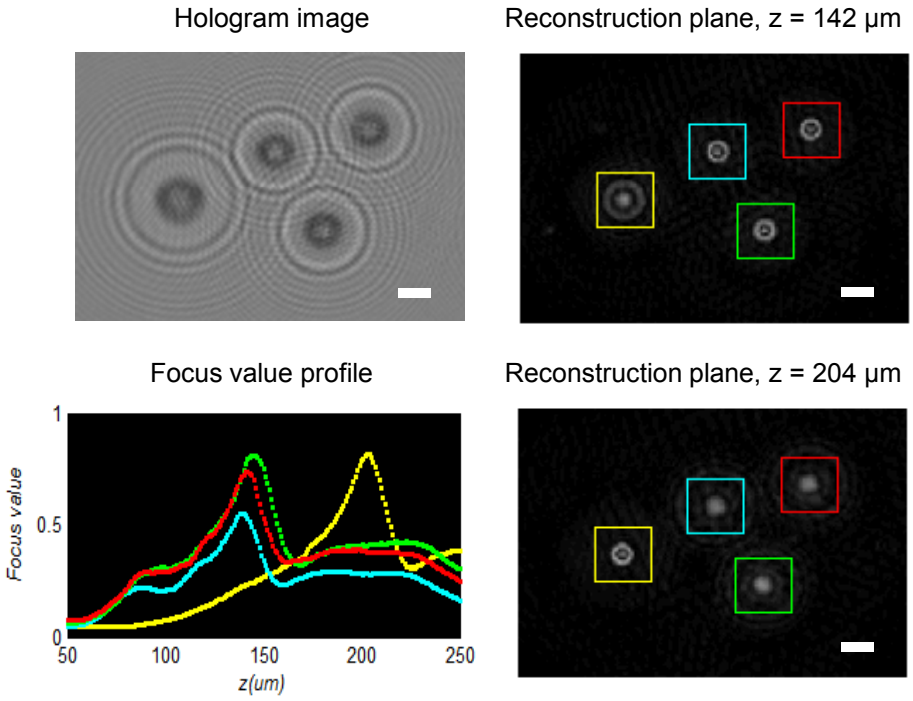


**Figure S7.** Typical hologram image of 7 μm particles processed in this study and its reconstructed images at different depthwise positions. Each particle is optimally focused at a certain $z$-position where the corresponding focus value becomes the maximum (see Movie 1 in ESI). Each particle and its focus value profile are represented by the same color. Scale bar: 10 μm.

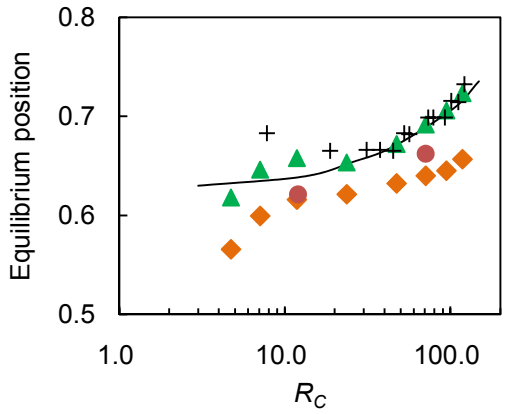


**Figure S8.** Equilibrium particle positions according to $R_C$. △, $a/H$ = 0.075 (present); ○, $a/H$ = 0.12 (present); ◇, $a/H$ = 0.16 (present); +, $a/H$ = 0.071 (Kim and Yoo [5]); —, asymptotic line for a channel flow (Matas et al. [6]).

## SI Text

### Digital holographic microscopy

A single beam in-line digital holographic microscopy technique which utilizes an objective lens was adopted in this study [1]. This method relieves the pixel-size limitations of the image sensor array and greatly increases the spatial resolution of digital holograms by magnifying the hologram image. As a result, the measurement accuracy of the system along the light propagation direction can be largely enhanced. In this technique, a coherent planar light wave irradiates the particles as a reference wave and the superposition of the unaffected reference wave and the wave diffracted by a particle (object wave) makes fringes (i.e., hologram) on the focal plane of the objective lens. Then the hologram image is magnified on the image plane and recorded by digital camera as a digital image (Fig. S5).

### Numerical reconstruction of hologram

Before the numerical reconstruction of holograms, the background image was subtracted from raw hologram images. The background image of each hologram was obtained by taking the pixel-by-pixel median of seven consecutive hologram images acquired sequentially. This process successfully removed the temporal and spatial background variations and increased the SNR of the hologram.

The background subtracted hologram image was then numerically reconstructed to analyze the 3D position information of the object by employing the Fresnel-Kirchhoff diffraction formula [2]. This consists of the convolution between the hologram function $h(x,y)$ and the diffraction kernel $g(x,y)$ at each reconstruction plane as follows:

$$\Gamma(\xi,\eta)=\frac{i}{\lambda}\int_{-\infty}^{\infty}\int_{-\infty}^{\infty}\mathrm{E}_R(x,y)h(x,y)\frac{\exp\left(-i\frac{2\pi}{\lambda}\rho\right)}{\rho}dxdy \tag{S1}$$

with

$$\rho=\sqrt{d^2+(\xi-x)^2+(\eta-y)^2}\,. \tag{S2}$$

Here, $\rho$ is the distance between a point in the hologram plane and a point in the reconstruction plane. The coordinate systems adopted in the numerical reconstruction are shown in Fig. S6. Eq. S1 calculates the complex amplitude of the reconstructed wave field propagated by a distance $d$ from the hologram plane. Hence, in order to reconstruct the volume information of the object field, one needs to calculate the whole reconstruction slices in the volume with varying the reconstruction distance $d$.

It is notable that if a planar light wave is used for the reference wave $\mathrm{E}_R(x,y)$, it is simply given by the real amplitude:

$$\mathrm{E}_R=a_R+i0=a_R \tag{S3}$$

which can be neglected in the numerical reconstruction. Hence, the Fresnel-Kirchhoff integral of Eq. S1 can

be interpreted as a convolution of the hologram function $h(x,y)$ and diffraction kernel $g(x,y)$:

$$\Gamma(\xi,\eta)=\{h(x,y)\otimes g(x,y)\}(\xi,\eta) \tag{S4}$$

with

$$g(x,y)=\frac{i}{\lambda}\frac{\exp\left(-i\frac{2\pi}{\lambda}\sqrt{d^2+x^2+y^2}\right)}{\sqrt{d^2+x^2+y^2}}. \tag{S5}$$

From the convolution theorem, it can be efficiently calculated by employing the two-dimensional fast Fourier transforms (FFTs) as follow:

$$\Gamma(\xi,\eta)=\Im^{-1}\left[\Im\{h(x,y)\}\Im\{g(x,y)\}\right] \tag{S6}$$

where $\Im$ and $\Im^{-1}$ denote the FFT and inverse-FFT, respectively. The intensity field of the reconstructed images can be obtained by taking the absolute $|\Gamma(\xi,\eta)|$. Here, it should be noted that the FFT of hologram function $h(x,y)$ is performed just once at the beginning of reconstruction procedure. In addition, the FFT routine for the diffraction kernel can be eliminated by adopting the analytical solution which is given from the angular spectrum analysis [3]:

$$\Im\{g(x,y)\}=G(f_x,f_y)=\exp\left\{i\frac{2\pi}{\lambda}d\sqrt{1-(\lambda f_x)^2-(\lambda f_y)^2}\right\}. \tag{S7}$$

In this equation, $f_x$ and $f_y$ represent the spectral coordinates. Hence, one may note that only one inverse-FFT is needed to reconstruct the complex wave field at any different plane of *z* separated by *d* from the hologram plane. Moreover, as the algorithm preserves a constant scale in the reconstructed image with the hologram image, it is particularly suitable for the volumetric flow measurement.

It is worth to note that the Fresnel approximation has been commonly used for holographic reconstruction in many previous studies owing to its superior computational efficiency with the approximation of a spherical Huygens wavelet as a parabolic surface [2, 4]. However, the angular spectrum analysis employed in this study not only provide fairly good computational efficiency, but also gives higher degree of accuracy since it does not require any simplifications such as the Fresnel approximation.

### Determination of 3D particle position

After the numerical reconstruction procedure of each hologram image, the 3D positions of the particles embedded in the reconstructed images were determined. Each reconstructed image contains slice information of the volume of interest. To find the in-plane (*x*, *y*) positions of the particles, whole reconstructed images were projected into one image (projection image) to get the maximum intensity distribution, since the reconstructed particles have higher intensity values than the background. Then a band-pass filter and a local-peak-searching algorithm were applied to the projection image to locate the in-plane center position of each particle.

After locating the in-plane position of each particle, a list of rectangular section enclosing each particle was generated by segmenting the particles in the projection image. Here, a rectangular shape was adopted for the ease of image handling. The size of each segment was determined to hold the whole neighboring pixels which exceed 80% intensity of the particle center in the projection image. Then each reconstructed image was cropped with the rectangular sections, and the corresponding focus value of each section was calculated by adopting an autofocus function. This process generated a list of focus values along the depthwise direction for each particle. The focus value of a particle typically increases as the reconstruction plane approaches the actual particle position because the focused real images are maximized and the unfocused images are minimized at the plane where the particle is located. Hence, the *z*-position of each particle can be regarded as the peak position of each focus value profile. For the autofocus function, we used the two-dimensional image variance which is defined as follow:

$$VAR(z) = \frac{1}{N_x N_y} \sum_{x,y} \left\{ I(x,y;z) - \bar{I}(z) \right\}^2 \tag{S8}$$

where, $I$ and $\bar{I}$ are the intensity distribution and its mean, respectively. $N_x$ and $N_y$ represent the image pixel dimensions. We compared several autofocus functions in preliminary tests and found that this function is most robust, especially for large-sized particles. The typical example of the focus value profiles obtained from the reconstructed particle images are presented in Fig. S7 and Movie 1.

## Equilibrium position

The lateral equilibrium positions were determined by taking the Gaussian estimation around the peak in the lateral PDF distribution. The resulting equilibrium positions are depicted in Fig. S8 with those of Kim and Yoo [5] and the asymptotic theory of Matas et al. [6]. The equilibrium position shifts outward with increasing the channel Reynolds number $R_C$ as reported in several previous studies [5-8]. The smaller particles agree well with the theoretical result because the asymptotic theory assumed the particle to be infinitesimal in size [6-8]. When the particle size is increased, the equilibrium position shifts toward the centerline and the deviation from the theoretical line increases. It can be explained by the increase of shear-gradient in the gap between the particle surface and the wall. The increase of particle size increases the shear gradient in the gap because the wall-to-wall (particle surface) distance is accordingly decreased. It is known that a larger shear-gradient in the thin fluid layer between the particle and the wall induces a stronger repulsion force due to the enhanced lubrication effect [9]. On the other hand, it should also be noted that the equilibrium position maintains a constant value with increasing the entry length $L_E/H$ when the value of $R_C$ and the particle size ratio $a/H$ are fixed. This indicates that the equilibrium position is a function of $a/H$ and $R_C$ only and not affected by $L_E/H$ when the inertial migration is fully developed.

## References

[1] J. Sheng, E. Malkiel, and J. Katz, “Digital holographic microscope for measuring three-dimensional

particle distributions and motions," *Appl. Opt.*, **45**, 3893-3901, 2006.

[2] U. Schnars and W. Jueptner, *Digital holography*, Springer, Berlin, 2005.

[3] J. W. Goodman, *Introduction to Fourier optics*, McGraw-Hill, New York, 1996.

[4] S. Murata and N. Yasuda, "Potential of digital holography in particle measurement," *Opt. Laser Tech.*, **32**, 567-574, 2000.

[5] Y. W. Kim and J. Y. Yoo, "The lateral migration of neutrally-buoyant spheres transported through square microchannels," *J. Micromech. Microeng.*, **18**, 065015, 2008.

[6] J. Matas, J. F. Moris and E. Guazzelli, "Inertial migration of rigid spherical particles in Poiseuille flow," *J. Fluid Mech.*, **515**, 171-195, 2004.

[7] J. A. Schonberg and E. J. Hinch, "Inertial migration of a sphere in Poiseuille flow," *J. Fluid Mech.*, **203**, 517-524, 1989.

[8] E. S. Asmolov, "The inertial lift on a spherical particle in a plane Poiseuille flow at large channel Reynolds number," *J. Fluid Mech.*, **381**, 63-87, 1999.

[9] J. Feng, H. H. Hu and D. D. Joseph, "Direct simulation of initial value problems for the motion of solid bodies in a Newtonian fluid," *J. Fluid Mech.*, **277**, 271-301, 1994.